Functionalization of indium oxide for empowered detection of CO_2 over an extra-wide range of concentrations

A. Rossi[1*], B. Fabbri[1], E. Spagnoli[1], A. Gaiardo[2], M. Valt[2], M. Ferroni [3,4], M. Ardit[1], S. Krik[5], A. Pedrielli[2], L. Vanzetti[2], V. Guidi[1]

[1] Department of Physics and Earth Sciences, University of Ferrara, Via Saragat 1, Ferrara 44122, Italy
[2] MNF- Micro Nano Facility, Sensors and Devices center, Bruno Kessler Foundation, Via Sommarive 18, Trento 38123, Italy
[3] Institute for Microelectronics and Microsystems IMM-CNR, via Gobetti 101, 40129 Bologna, Italy
[4] Department of Civil, Environmental, Architectural Engineering and Mathematics (DICATAM) Università degli Studi di Brescia - Via Branze, 43 - 25123 Brescia
[5] Sensing Technologies Lab, Faculty of Engineering, Free University of Bozen-Bolzano, Piazza Università 5, Bolzano 39100, Italy

Abstract:

Carbon capture, storage and utilization have become familiar terms when discussing climate change mitigation actions. Such endeavors demand the availability of smart and inexpensive devices for CO_2 monitoring. To date, CO_2 detection relies on optical properties and there is a lack of devices based on solid-state devices, which can be miniaturized and easily made compatible with IoT platforms. With this purpose, we present an innovative semiconductor as functional material for CO_2 detection. Nanostructured In_2O_3 films, functionalized by Na, proves to enhance the surface reactivity of pristine oxide so much that even rather stable a molecule as CO_2 is reduced. An advanced *operando* equipment based on surface-sensitive diffuse infrared Fourier transform is used to investigate its improved surface reactivity. The role of sodium is to increase the concentration of active sites such as oxygen vacancies and, in turn, to strengthen CO_2 adsorption and reaction at the surface. It results in a change in film conductivity, i.e., in transduction of a concentration of CO_2. The films exhibit excellent sensitivity and selectivity to CO_2 over an extra-wide range of concentration (250-5000 ppm), which covers most indoor and outdoor applications with marginal influence by environmental humidity.

* Corresponding author. Tel. +39 0532 974283
Email address: arianna.rossi@unife.it

Keywords: CO_2 detection, chemically active metal oxides, In_2O_3, *operando* spectroscopies, smart sensors for IoT

1. Introduction

In recent years, with the development of industry and exponential urbanization, the problems of air pollution and global warming have become increasingly serious and gas monitoring has attained a sufficiently wide market to be commercially attractive. Carbon dioxide (CO_2) is

considered as the most important contributor to global warming, accounting for 76% of greenhouse effect [1,2], with an average global concentration level of 420 parts per million (ppm) [3]. Besides, recent research highlighted that people spend more than 90% of their time in indoor environments [4] and, consequently, are subjected to breath CO_2 concentrations higher than environmental background up to several thousand ppm, depending on the occupancy and ventilation of the confined space [5]. Indeed, high concentrations of indoor CO_2 have been linked to a deleterious health effect, such as the Sick Building Syndrome (SBS) [6]. In particular, long exposure to concentrations ranging between 2000 and 5000 ppm negatively affects cognitive performance, including headaches and loss of attention [7]. Severe toxicity and oxygen deprivation effects occur as CO_2 concentration exceeds 5000 ppm over an 8-h workday [8].

Moreover, as recently reported by Peng and Himenez (2021), CO_2 was pointed out as an indicator for indoor ventilation and in turn of pathogen infection (e.g., SARS-CoV-2) probability through aerosol transmission [9]. Monitoring CO_2 concentration could be useful in greenhouse planting (where CO_2 concentration is usually kept below 300 ppm) and in packaging for fruits and vegetables conservation (up to 25%) [10,11].

For CO_2 measurements, several techniques have been developed, spanning from analytical instruments such as gas chromatography (GC) assisted by mass spectrometry (MS), infrared spectroscopy (IR) to compact and portable devices, i.e., optical, acoustic, electrochemical, capacitive, and non-dispersive infrared based sensors (NDIR). However, some limitations, e.g., lack of portability, high-maintenance cost, need for trained users (for GC-MS), short device lifetime (for optical and electrochemical sensors), low selectivity (for acoustic sensors) and spectral interference (for NDIR sensors) have prevented CO_2 monitoring on a large scale [12–15].

Hence, alternative systems combining accuracy, resolution and robustness with small size, low cost and power consumption would be highly demanded. Solid-state gas sensors, such as chemoresistive devices, would represent a viable route in this sense to previously mentioned tools, because such devices could be easily integrated in Internet of Things (IoT) networks. Among them, metal-oxide (MOX) based gas sensors have gained a wide market due to high sensitivity, rapid response, stability, and reproducibility combining simple and low-cost fabrication methods. Unfortunately, to date they have exhibited a modest attitude to detect CO_2, resulting in poor response due to the inherent stable nature of such molecule [16–21].

Therefore, new functional materials for CO_2 sensing featuring stronger chemical reactivity, while maintaining complete reversibility of the detection process, represent a challenge. MOXs are an interesting class of semiconductors, as their properties can be engineered by changing the chemical-physical composition of the metal oxide, i.e., the crystal structure, the size and shape at the nanostructure level, or by introducing additives (main-group elements, transition metals, noble metals, etc.) [22,23]. In particular, dopant metal oxides proved effective to enhance chemical reactivity [24]. Recently, it was discovered that alkali metals act as catalysts to promote analyte adsorption at the compound surface [25]. In fact, they accelerate the formation and facilitate the stabilization of reaction intermediates, ultimately increasing the adsorption of CO_2.

Indium oxide (In_2O_3) has been studied in electrochemistry as an efficient catalyst for CO_2 hydrogenation to methanol [26]. The basic idea behind this investigation is to merge the concepts

of above, i.e., develop a sodium-doped of indium oxide semiconductor (Na:In_2O_3) to achieve high CO_2 sensing. Indeed, In_2O_3 is not a novelty among MOX sensors, inasmuch as its detection properties have already been probed vs. ozone, nitrogen dioxide and methane [27–29]. In sight of potential large-scale application, we resorted to a simple synthesis method such as sol-gel process. The powders, conveniently characterized, were used as a functional component for screen-printed sensing films and probed vs. different concentrations of CO_2 and its potential interfering gases (toluene, ethanol, carbon monoxide, and nitrogen dioxide) for applications. The sensing capability vs. CO_2 was explored over a wide range of concentrations (250-5000 ppm), covering most relevant indoor and outdoor applications. The role of the sodium in the sensing mechanism was investigated through Fourier transform infrared diffuse reflectance (DRIFT) spectroscopy, an *operando* characterization technique to monitor the gas-solid interaction occurring at the surface while the sensor is being working [30–32].

2. Results and Discussion

In this study, we synthesised pristine and Na-doped indium oxide by means of sol-gel process, as detailed in the Experimental Section. Morphology, elemental composition, and structure of the nanopowders were investigated by scanning electron microscopy (SEM), transmission electron microscopy (TEM), energy dispersion x-ray (EDX) analysis and X-ray diffraction (XRD). The doping effect of sodium incorporation in the indium oxide nanostructure was derived from the optical properties obtained by X-ray photoelectron spectroscopy (XPS) and UV-visible spectroscopy (UV-vis). Then, sensing devices were produced by a scalable and controllable fabrication technique such as screen printing. The sensors based on pristine and Na-doped indium oxide were electrically characterized to study their sensing performance. Finally, the impact of sodium addition on the latter was investigated through *operando* DRIFT spectroscopy.

2.1. Powder Characterization

The XRD pattern of the same powder revealed that both the pristine and Na-doped sample are monophasic and with a cubic crystal structure (s.g. *Ia-3*) (**Figure 1a**). The diffraction peaks for Na:In_2O_3 were shifted slightly towards 2θ values lower than those for the pristine In_2O_3, indicating lattice expansion through sodium doping. Along with a lattice parameters variation, the addition of sodium yielded a crystal structure that has nearly the same crystallite size (X_{XRD}), but a lower microstrain (e_0), as provided in **Table 1**. Namely, peak broadening effects which may arise from dislocations or interstitial, substitutional, and other similar point defects as determined by XRD analyses [33] are hindered by sodium doping.

Table 1. Main crystallographic information (i.e., crystal system, space group, lattice parameter (*a*), crystallite size (X_{XRD}) and microstrain (e_0)) for the investigated samples.

Sample	Crystal System	Space Group	*a* [Å]	Crystallite size, X_{XRD} [nm]	Microstrain $e_0 \times 100$
In_2O_3	In_2O_3 (cubic)	Ia-3	10.1193(4)	10.4(1)	0.101(2)
Na:In_2O_3	In_2O_3 (cubic)	Ia-3	10.1213(2)	10.9(1)	0.060(3)

The SEM analysis on the In_2O_3-based powders showed regular nanometric spherical particles with equiaxed shape (**Figure S1 and S2a, Supporting Information**). The morphology of Na:In_2O_3 was further characterized by TEM. **Figure 1b** confirmed that the powder consisted of monodisperse nanoparticles and averaged 11±3 nm in size. Here, crystalline facets were highlighted on the particles with round shape (see **Figure 1c**). The particles were crystalline as no amorphous or secondary segregated phases were observed at the grain surface. Selected-area electron diffraction (SAED) pattern (**Figure S3, Supporting Information**) showed the typical interplanar distances of the cubic phase of In_2O_3, the major reflections of which derive from crystalline planes (222), (004) and (044), then confirming XRD results. Furthermore, scanning transmission electron microscopy combined with energy dispersive x-ray analysis (STEM-EDX) analysis confirmed the localization of Na within the nanometric In_2O_3 particles (**Figure S4, Supporting Information**).

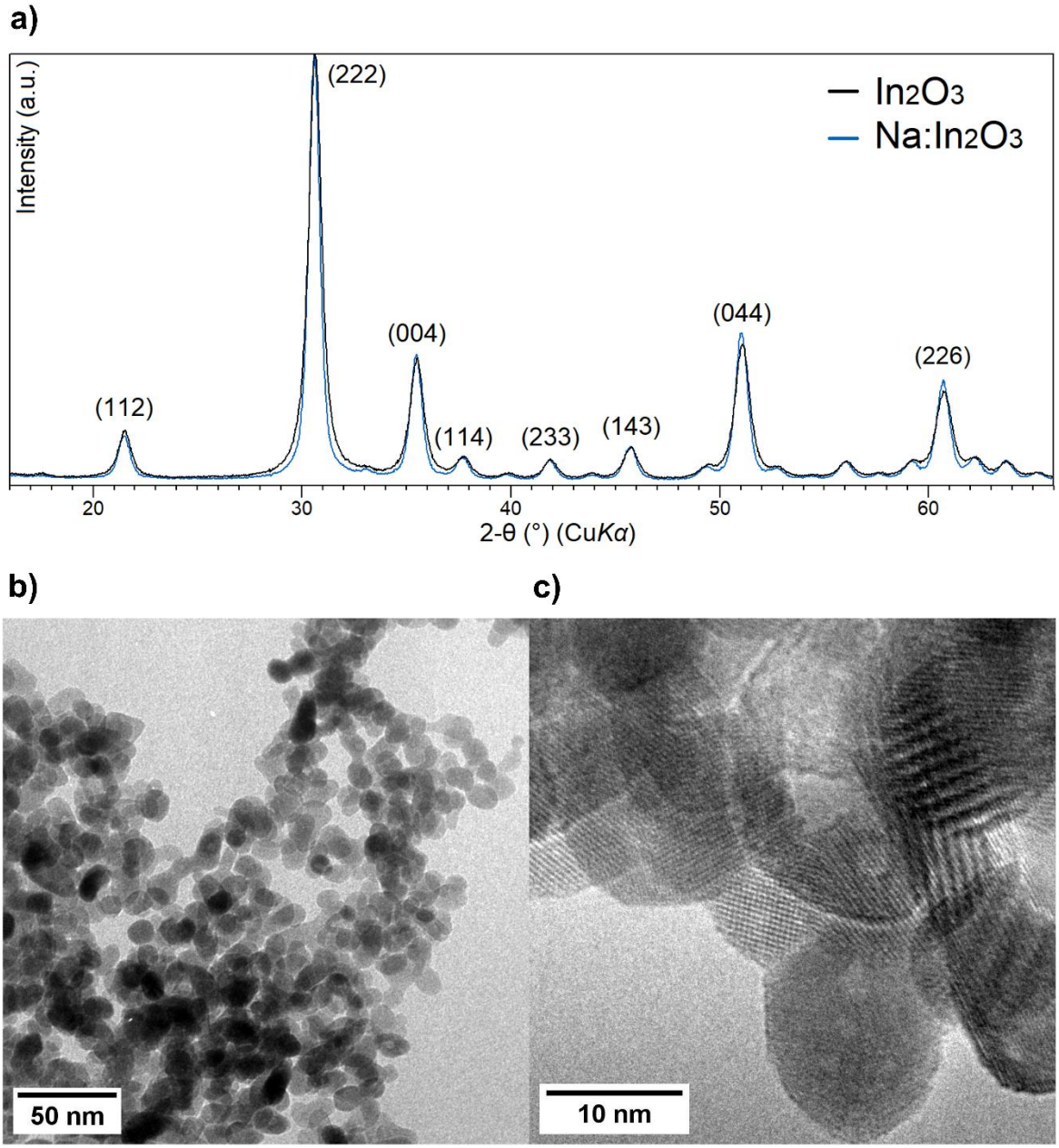

Figure 1. a) XRD pattern of pristine In_2O_3 and Na:In_2O_3 powder. b) and c) HR-TEM images of Na:In_2O_3 powder.

The survey spectrum of high-resolution XPS over the powders (**Figure 2)** revealed the presence of three main elements, i.e., In, O and Na. To investigate the chemical state of these elements, high resolution spectra of In 3d (440-455 eV), O 1s (526-535 eV) and Na 1s (1066-1075 eV) core levels were collected. Their quantification (atomic%) in the pristine and doped samples is reported in **Table S1**. **Figure 2a** compares the XPS spectrum of the In 3d core level for the powders with and without Na, which neatly shows the doublet corresponding to $3d_{5/2}$ and $3d_{3/2}$. For pristine In_2O_3 sample, In $3d_{5/2}$ and In $3d_{3/2}$ peaks appeared at 444.1 eV and 451.6 eV, respectively. The energy of the In 3d doublet corresponds to In^{3+} oxidation state and In-O bonds [34]. A slight change of binding energies of the In 3d peaks was observed between pristine In_2O_3 and Na:In_2O_3 samples. The displacement of these peaks indicates different chemical

neighborhoods due to incorporation of sodium into the In_2O_3 lattice. Then, a similar shift can be also observed for O 1s, as reported in **Table S2**. **Figure 2b and 2c** show a detailed deconvolution of O 1s high resolution spectra, both for Na:In_2O_3 and In_2O_3 samples, in four peaks corresponding to O lattice (In-O-In), O atoms adjoined to oxygen deficiency sites (oxygen vacancies), surface hydroxyl groups OH-In, and H_2O (~533.0 eV) [35–37]. The main O 1s peak, at 529.6 eV for In_2O_3 (529.2 eV for Na:In_2O_3), corresponds to the O lattice. The binding energies at 530.3 eV for In_2O_3 (529.9 eV for Na:In_2O_3) are assigned to O atoms adjoined to oxygen vacancies, while O 1s peak at 531.4 eV for In_2O_3 (531.1 eV for Na:In_2O_3) is related to the adsorbed -OH terminations [38,39]. The increased % of O atoms adjoined to oxygen vacancies found in the doped In_2O_3 sample suggests a higher concentration of oxygen vacancies for Na:In_2O_3 than In_2O_3. Although the quantification of the total amount of oxygen vacancies in indium oxide by XPS analysis can be hardly deduced from the fit of the O 1s peaks, the assessment is supported by the different ratio between oxygen and metals (In + Na) in the two samples, equal to 1.22 and 1.32 for Na:In_2O_3 and In_2O_3, respectively (**Table S1**).
Figure 2d shows the high resolution spectrum of Na 1s core level in the Na:In_2O_3 powder. The binding energy identified at 1071.4 eV is ascribed to Na^+ [40], which confirmed the successful incorporation of Na into the In_2O_3 lattice through sol-gel synthesis. Therefore, doping with low-oxidation-state alkali metals is a suitable strategy to promote the formation and to control the concentration of oxygen vacancies in MOX, enabling the tuning of catalytic and optoelectronic properties, as already observed in previous works [41,42].

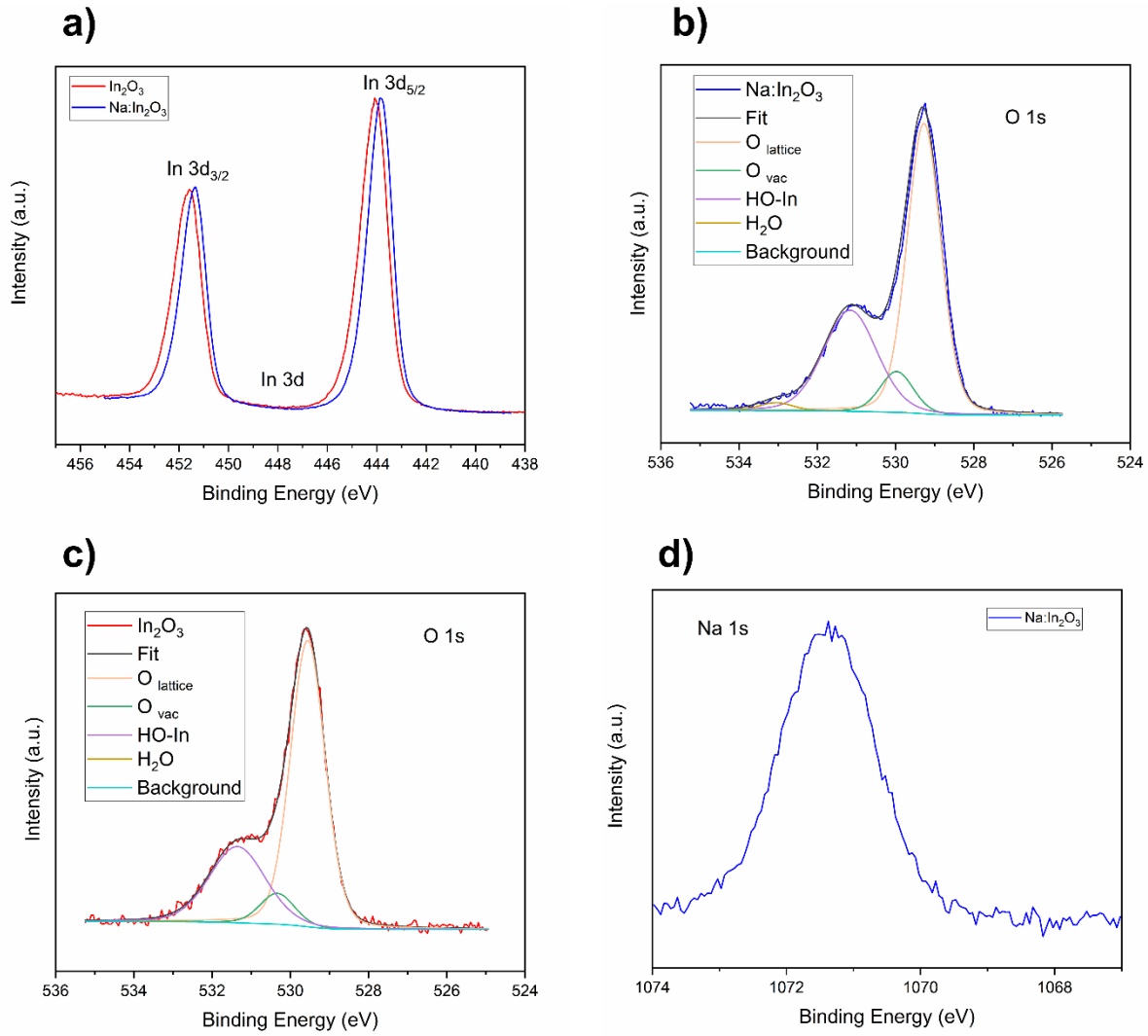

Figure 2. High-resolution XPS spectra of a) In 3d, b) and c) O 1s and (d) Na 1s core levels of $Na:In_2O_3$ (blue line) and In_2O_3 powders (red line).

The optical properties of the In_2O_3-based nanopowders were characterized by UV and visible spectroscopies (**Figure 3**). It can be observed that the maximum in absorption spectrum for pristine In_2O_3 was recorded at a wavelength of about 304 nm. For comparison, the maximum for doped In_2O_3 was red-shifted to 313 nm. Specifically, the optical absorption of the powders was investigated to account for the influence of sodium to the direct band gap (E_g) of In_2O_3. This latter was determined by using Tauc's plot [43], resulting in E_g= 3.60 eV and 3.46 for the pristine In_2O_3 and $Na:In_2O_3$, respectively. This observation confirmed the role of sodium as dopant (Na^+). In fact, if sodium had been present in the sample as metallic (Na^0), no decrease in the bandgap width would have been observed [44,45]. This decrease in the bandgap confirms the role of Na^+ cations as an electrically active dopant in In_2O_3.

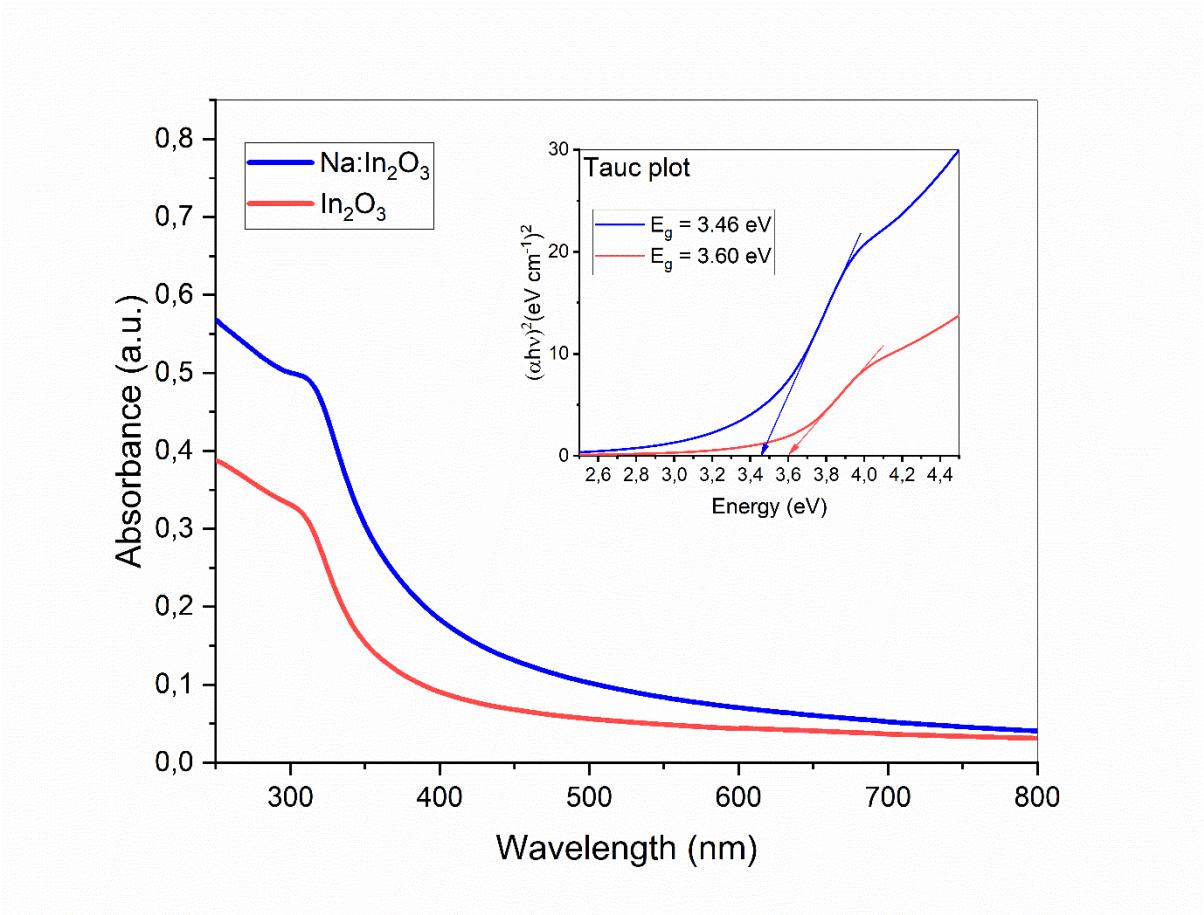

Figure 3. UV–visible absorbance spectrum and inset of $(\alpha h\nu)^2$ vs. energy (eV) for Na:In_2O_3 and In_2O_3.

2.2. Gas sensing performance

The gas response of the films based on pristine In_2O_3 and Na:In_2O_3 was investigated by measuring the conductance change at different working temperatures (150-450 °C) under exposure to 500 ppm of carbon dioxide. As shown in **Figure S5a and S5b (Supporting Information)**, the optimal working temperature for Na:In_2O_3 film lay in the range 200-250 °C while the In_2O_3 film peaked at 250 °C. In the present work, to meet the demand for lowest power consumption, an operating temperature of 200 °C was chosen hereinafter for Na:In_2O_3. As expected, the conductance change after the injection of reducing gas such as carbon dioxide (**Figure S5c)** increased for both In_2O_3 and Na:In_2O_3, owing to their n-type behavior. Then, the sensor responses were calculated using **Equation 11** [46].

The sensitivity to carbon dioxide was investigated by measuring the conductance of Na:In_2O_3 film when exposed to 250, 500, 1000, 2000, 3500 and 5000 ppm of CO_2, as compared to that for pristine In_2O_3. The gas concentration range was selected to probe the sensor for operation in both indoor and outdoor applications [11,47,48]. As it can be seen in **Figure 4**, the response of Na:In_2O_3 film gradually increased from 4.33 at 250 ppm to 12.7 at 5000 ppm, featuring remarkable sensitivity that envisages noteworthy potential for CO_2 monitoring in several contexts. In contrast, the response of pristine In_2O_3 film was much lower than for the doped film and, above all, with strong tendency to saturate even at the lowest concentrations.

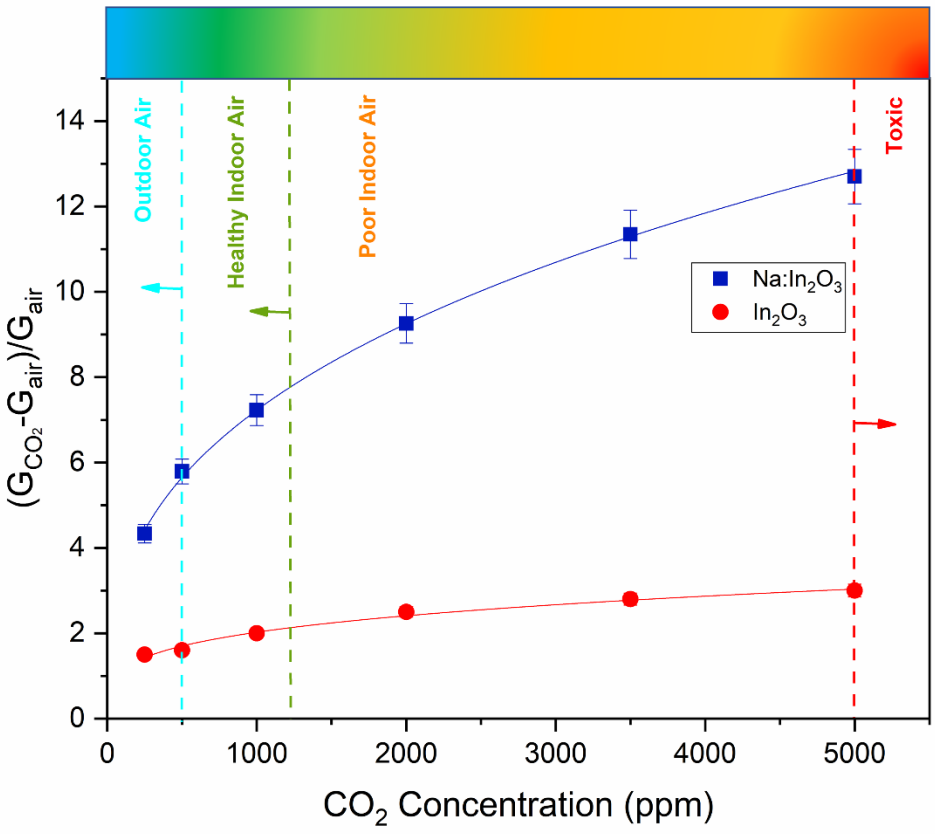

Figure 4. Calibration curves of Na:In_2O_3 and pristine In_2O_3 sensors at 200 °C and 250 °C, respectively, for carbon dioxide.

The film response also proved to be repeatable (see **Figure 5**), as requested for application as a sensor. The response τ_{res} and recovery τ_{rec} times were determined to be 5 (3) min and 9 (23) min, respectively, at 400 (1200) ppm. The kinetics of the reaction mechanism could be accelerated by increasing the working temperature, however already at this level, the sensors are adequately prompt to address indoor and outdoor applications.
Response and recovery times of the order of ten minutes are typical characteristic timing for other MOX semiconductors in previous works [49–51].

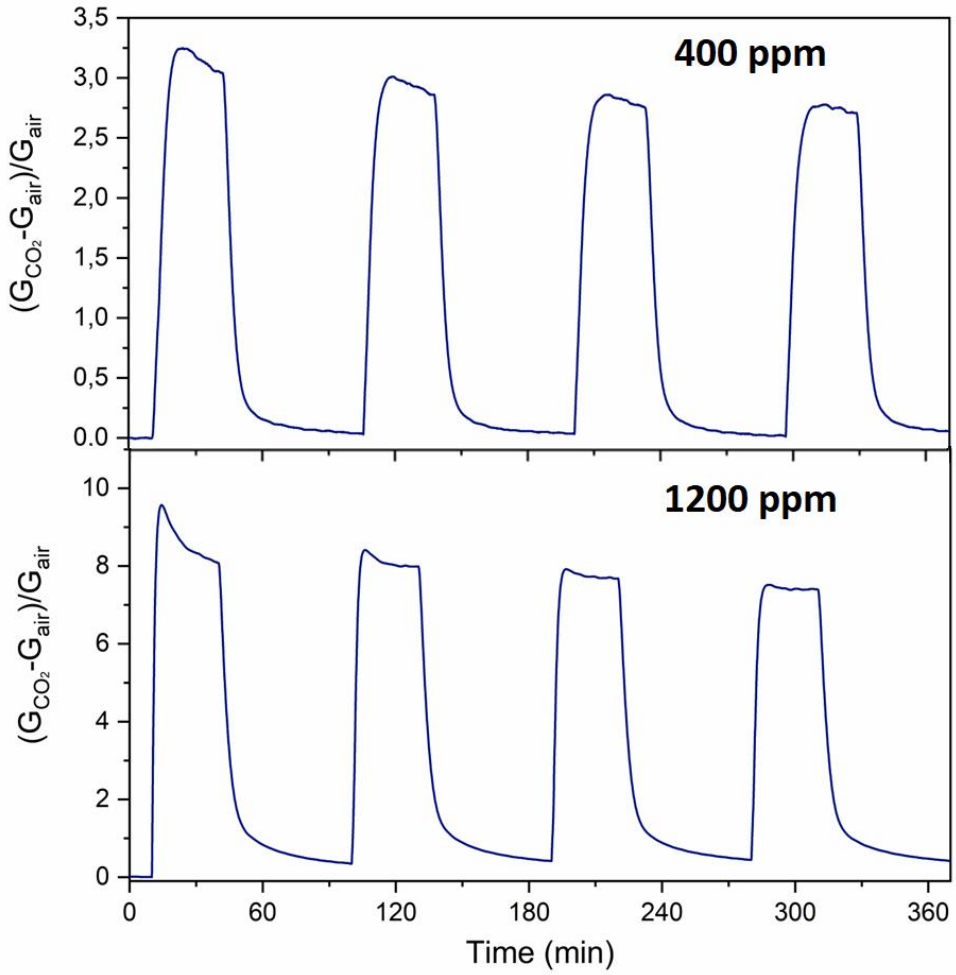

Figure 5. The 4-cycle repeatability test as a function of time. For these experiments, Na:In_2O_3 sensor was exposed towards 400 and 1200 ppm of carbon dioxide gas.

Under dry condition, n-type semiconductors form an electron depletion region near the surface due to adsorption, dissociation, and ionization of environmental oxygen in the operating temperature range of 200–500 °C, which leads to decreasing the sensor conductance. Thus, a chemical reaction between the negatively charged surface oxygen and any reducing gaseous analyte releases electrons to the conduction band (CB) resulting in an increase of the film conductivity. Under wet conditions, the conductance of a MOX semiconductor is affected by the dissociation of water vapor on the surface forming protons and hydroxyl groups, **Equation 1** [52]. Protons react with chemisorbed O^- species forming neutral -OH groups, thus affecting the conductance.

$$H_2O \rightarrow H^+ + OH^- \quad (1)$$

On the other hand, OH^- replaces the coverage of O^- species, passivating the film adsorption sites for detection of analytes. Moreover, in a humid environment, the gas sensing response of a MOX semiconductor is attributable to the competition between the adsorption/desorption processes of H_2O molecules and the analyte.

In this study, the Na:In_2O_3 sensor was exposed to 500 ppm of carbon dioxide at different RH levels (3-64%). As shown in **Figure S6 (Supporting Information),** with an increase of relative humidity, the baseline of film conductance also increased due to the formation of the -OH groups. With the injection of carbon dioxide, competition for the active sites may occur between water vapor and the target gas. Hence, the combination of such competitive interactions resulted in substantial change in film conductance. Indeed, in presence of humidity, the sensor exhibited lower response (**Equation 12**) to CO_2 than in dry condition (**Figure 6a**). It is worthwhile noticing that the response is marginally affected by humidity over a wide range, which is a key-feature for possible applications. By contrast, **Figure 6a** shows that undoped In_2O_3 film response merely vanishes under wet conditions.

Moreover, in practical implementation of a sensing unit vs. an analyte of interest, one should consider the co-presence of other gases whose physico-chemical properties may affect the sensor response. Therefore, Na:In_2O_3 film selectivity was explored by exposing the sensors to various interferents, such as ethanol, toluene, NO_2 and CO at different concentrations (**Figure 6b**). These were selected in sight of indoor and outdoor air quality monitoring, according to the concentration of interest reported by The National Institute for Occupational Safety and Health (NIOSH) and American Society of Heating, Refrigerating and Air-Conditioning Engineers (ASHRAE) [53–56].

It turned out that the Na-doped sensor showed better responses than the pristine In_2O_3 sensor for all the gases tested. In particular, we estimated the selectivity coefficient (k_s) [52] of the sensors for CO_2 detection (**Table S3, Supporting Information**). Hence, the results obtained make the achieved sensor attractive for various CO_2 applications, since it is not significantly affected by the influence of other interfering gases.

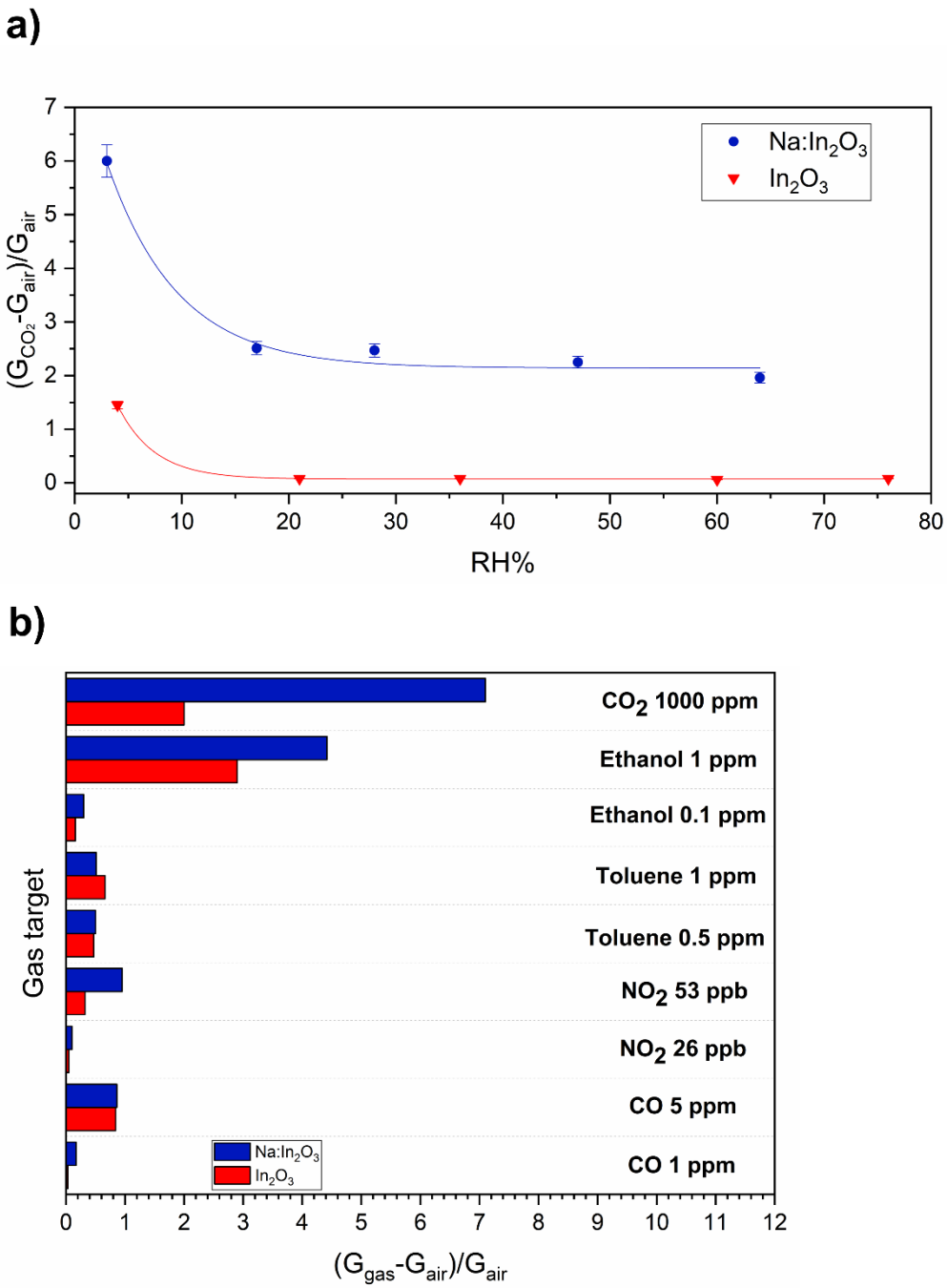

Figure 6. a) Influence of RH% on the response to 500 ppm of carbon dioxide for Na:In_2O_3 and pristine In_2O_3 sensors. b) Selectivity of In_2O_3-based films toward different analytes.

To further evaluate the features of the Na:In_2O_3 sensor proposed in this work, we compare its sensing performance vs. CO_2 to those of other MOX-based sensors, which have been reported in the literature so far (**Table 2**). The table below summarizes the investigations conducted on CO_2-sensitive materials operating at relatively low temperature and prepared by synthesis methods similar to the one used in this work.

It is noteworthy that the sensor in this work exhibits superior sensitivity vs. CO_2 while operating at relatively low temperature and above all is marginally affected by environmental humidity, paving the way to indoor and outdoor applications.

Table 2. Sensing parameters of different CO_2 sensors based on MOX semiconductors.

Sensing material	Synthesis route	Operating temperature [°C]	Response/Concentration [ppm]	Operating Condition	Reference
ZnO/CuO nanorods	Hydrothermal	RT	0.09/1000 [a]	Dry	[16]
5wt%Sn-CdO nanopowders	Co-precipitating	250	1.18/5000 [b*]	Dry	[17]
CuO@1wt%Ag-$BaTiO_3$ spheres decorated	Mixing	120	1.40/700 [a]	Dry	[18]
CeO_2 Yolk-shell nanospheres	Solvothermal	100	3.98/2400 [c]	Negligible response below 70 %RH	[19]
$Nd_2O_2CO_3$ nanoparticles	Sol-gel	350	4/1000 [d]	Negligible response below 50 %RH	[20]
CaO-In_2O_3 mesoporous	Impregnation	230	1.80/2000 [d]	Dry	[21]
N-ZnO nanoparticles	Sol-gel	250	4.5/2000 [d*]	Dry	[57]
Na:In_2O_3 nanoparticles	**Sol-gel**	**200**	**7.1/1000** [e]	**Uniform response above 15 %RH**	**This work**

[a] $R = \frac{Rgas - R\ air}{R\ air}$, [b] $R = \frac{R\ air - R\ gas}{R\ gas} x\ 100$, [c] $R = \frac{R\ gas}{R\ air}$, [d] $R = \frac{R\ air}{R\ gas}$, [e] $R = \frac{G\ gas - G\ air}{G\ air}$, where G is the conductance and R is the resistance. (G_{gas} and R_{gas}: conductance and resistance in CO_2 atmosphere; G_{air} and R_{air}: conductance and resistance in carrier gas).

*Denotes a value not explicitly stated in the study but approximated from a graphical plot.

2.3. Operando DRIFT investigation towards CO_2 detection

In order to elucidate the sensing mechanism that enables the electrical activity of the new material in presence of carbon dioxide, *operando* DRIFT measurements were performed. This advanced characterization technique provides an insight into the species adsorbed at the surface, aiding the analysis of the products formed as a result of chemical reactions.
It was first compared the behavior of Na:In_2O_3 to that of the pristine In_2O_3. Each sensor was exposed to synthetic dry air, to identify the species pre-adsorbed onto the material surface before supplying carbon dioxide. Single-channel spectra were collected while each sensor was being heated at the same working temperature of 200 °C in order to compare their sensing mechanism in the same thermodynamics conditions, **Figure S7 (Supporting Information).** Simultaneously the resistance of the sensing films was acquired.
Secondly, the sensors were exposed to 3500 ppm of CO_2 in dry condition **Figure S8a (Supporting Information).** Comparing the two sensors, there is the formation of bridged carbonates, bidentate for Na:In_2O_3 and inorganic carboxylates for In_2O_3. According to the

literature [58], the latter, due to their thermal stability, are less reactive with respect to the former species, and this is explanatory of limited electrical response of pristine In_2O_3 vs. CO_2.
The solid-gas kinetics occurring at the surface of Na:In_2O_3 sensor was investigated by acquiring DRIFT spectra at topic intervals while the dynamical response of the sensor vs. 1000 ppm CO_2 was being carried out (**Figure 7**). The figure highlights that adsorption and desorption are completely reversible at 200 °C. DRIFT spectra highlighted the presence of hydroxyl groups adsorbed on the surface during CO_2 injection (see step 2 and 3, **Figure 7**). According to [59], the sharp peak ca. 3711 cm^{-1} can be attributed to the formation of isolated hydroxyl groups, while the broad bands between 3640 and 3040 cm^{-1} are bridged hydroxyls. Both species are due to residual water vapor in the gas injection tube, see **Figure S9a (Supporting Information)**, and they decreased during the recovery to dry condition (see step 4, **Figure 7**). However, gaseous CO_2 molecules were the most abundant species observed by DRIFT [60]. As shown in **Figure 7b**, the presence of the characteristic peaks at ca. 2339 and 2365 cm^{-1} pertain to this molecule (see steps 2 and 3, **Figure 7**). The bands 1439 and 1034 cm^{-1} are assigned to In-O lattice vibrations overtones [61].
In the region between 1600 and 1000 cm^{-1}, there are two main carbonate species. Indeed, the exposure of the sample to CO_2 flow led to rapid formation of bidentate carbonate (b-HCO_3^-) as recorded by 1607 and 1291 cm^{-1} while bridged bidentate carbonate (br-CO_3^{2-}) were at 1564 cm^{-1} [62].
From the electrical point of view, the sensor resistance decreased with the injection of CO_2, due to carbonate species and hydroxyl groups formation (step 2 and 3, **Figure 7a**). On the other hand, film resistance increased as a result of CO_2 desorption (step 4 and 5, **Figure 7a**), which led to significant decrease in carbonate species while the bands corresponding to -OH groups remained almost constant in intensity owing to the lower working temperature (200 °C) which inhibited their desorption.

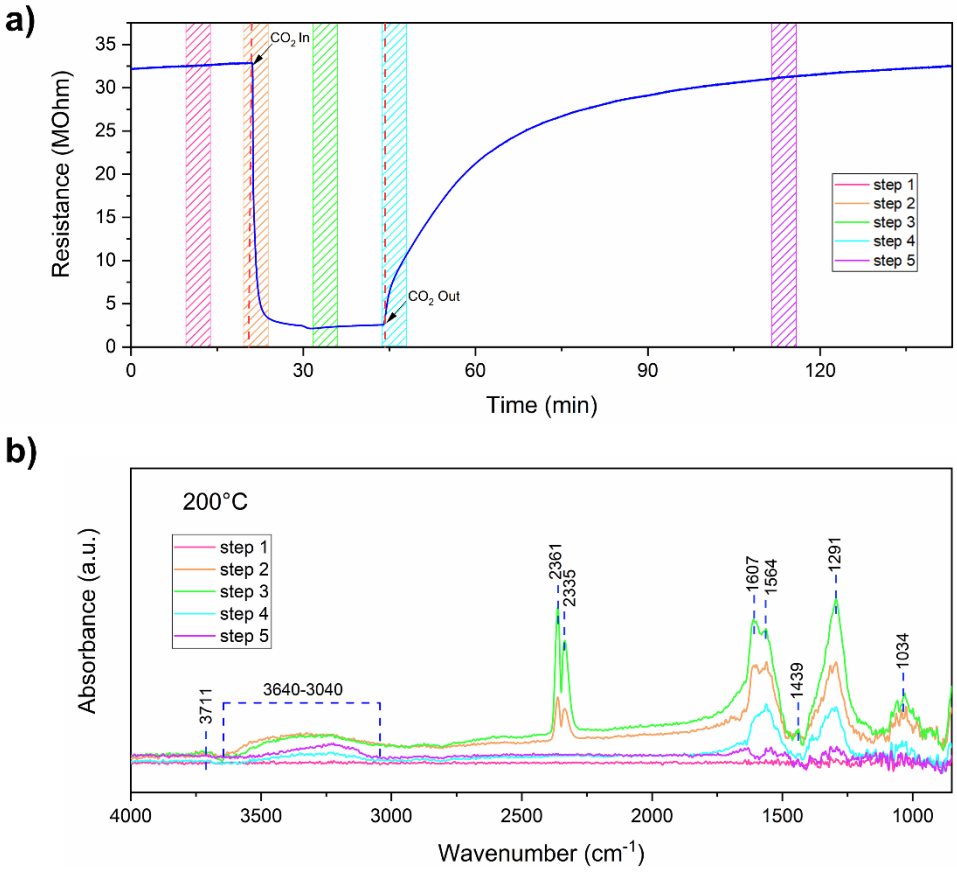

Figure 7. a) Measurement scheme, resistance change when the gas sensor was exposed to 1000 ppm of CO_2 in dry air at 200 °C with time intervals marked for FTIR spectrum sampling. b) Spectra acquired during CO_2 input and output under dry air conditions at time intervals marked above.

In order to further investigate the sensing mechanism towards CO_2, we compared DRIFT spectra acquired during the exposure to the two different concentrations of carbon dioxide (1000 and 3500 ppm) (**Figure S8b, Supporting Information**). At higher concentration, a slight increase in the intensities of all adsorbed species was recorded and two more peaks showed up at 3627 and 3600 cm^{-1}. According to the literature [62], they can be attributed to the ν(OH) modes of the newly formed hydroxyl groups of the bidentate carbonates and monodentate carbonates.

The stimulating behavior under humidity exposure we observed, led us to increase the relative humidity concentrations (5.5-22 RH%). Under wet environments in presence of 1000 ppm of CO_2 (see **Figure 8**), the DRIFT spectra can be explained in terms of chemical activity of three types of adsorbates on the surface, namely, $-CO_3^{2-}$, $-OH^-$, and $-O^-$ (see **Figure 8a**). The narrow and intense peaks between 4000-3300 cm^{-1} and 2100-1300 cm^{-1}, which increased with the humidity concentrations, are assigned to the gaseous H_2O molecules [63]. The competitive relation between hydroxyl groups and carbonate species became clear as an increase in the peaks due to hydroxyls groups resulted in a decrease of the carbonate species (see **Figure 8b**). Therefore, adsorbed H_2O on the surface limits the adsorption sites and inhibits the formation of carbonates [60].

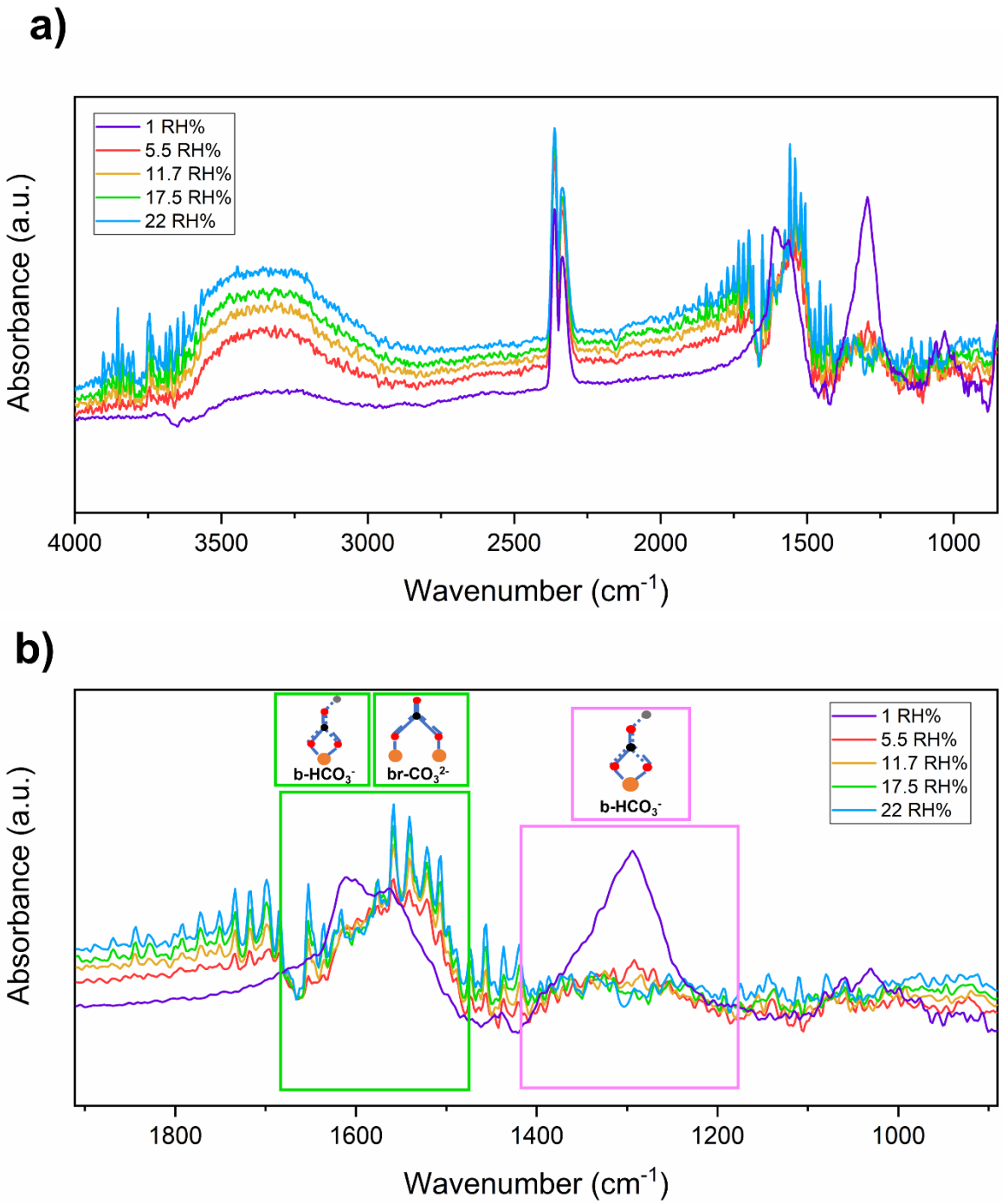

Figure 8. a) Spectra of Na:In_2O_3 film at 200 °C acquired during the inlet of 1000 ppm of CO_2 in dry conditions (1 RH%) and in wet conditions. b) Magnification of spectrum reported in (a) in the range from 2000 to 850 cm^{-1}. The spectral noise is related to the increase of water species adsorbed at the surface.

2.4. Sensing Mechanism

By combining the information obtained through DRIFT measurements with the electrical characterization of the film, it was possible to formulate some hypotheses about the detection mechanism of CO_2 by Na:In_2O_3 as a chemoresistive functional material. In particular, the sensing mechanism can be explained in terms of the band bending theory [64,65]. Considering dry air condition, at working temperatures ranging between 100 and 500 °C, the interaction of the sensing layer with atmospheric oxygen leads to ionosorption of the latter in molecular (O_2^-) and/or atomic (O^-, O^{2-}) species (see **Equation 2-5**) [66]. More precisely, the reactions occurring at the surface, listed as a function of increasing temperature, are the following:

$$O_2\,(gas) \leftrightarrow O_2\,(ads) \tag{2}$$

$$O_2\,(ads) + e^- \leftrightarrow O_2^-\,(ads) \tag{3}$$

$$O_2^-\,(ads) + e^- \leftrightarrow 2O^-(ads) \tag{4}$$

$$O^-(ads) + e^- \leftrightarrow O^{2-}(ads) \tag{5}$$

At an operating temperature of 200 °C, the oxygen ions (O^-) would dominate the ionosorption (**Equation 3 and 4)** [67]. As a result, atmospheric oxygen traps electrons from the CB, creating a potential barrier $(qV_s)_1$ and consequently increasing the resistance of the film with respect to room-temperature operation (*Stage I* in **Figure 9a**). As CO_2 is fed (*Stage II* in **Figure 9a**), its molecules react with the pre-adsorbed oxygen ions at the surface following **Equation 6** to produce carbonate ions and electrons [1,68].

$$CO_2\,(gas) + \frac{1}{\beta}\,O_\beta^{\alpha-}(ads) \leftrightarrow CO_3\,(ads) + \frac{\alpha}{\beta}\,e^- \tag{6}$$

Therefore, the concentration of free electrons in the CB of Na:In_2O_3 increases leading to a decrease in the potential barrier in this new state, $(qV_s)_2$, and consequently in the film resistance.

Under wet conditions, water molecules (**Equation 1**) both react with and hinder chemisorbed oxygens at the surface (*Stage I* in **Figure 9b**). This phenomenon influences the band bending effect, i.e., the potential barrier created in wet air is lower than in dry air ($(qV_s)_3 < (qV_s)_1$). This results in a decrease of the film resistance. Exposing the sensor to CO_2 in wet condition, hydroxyl groups promote the reaction in **Equation 7**, decreasing the potential barrier ($(qV_s)_4 < (qV_s)_3$) (*Stage II* in **Figure 9b**).

$$CO_2\,(gas) + OH^-(ads) \leftrightarrow HCO_3^-\,(surface) \tag{7}$$

However, higher water concentration hinders the reaction between active sites with CO_2. Therefore, the variation of potential barrier height with the exposure to the analyte is lower in wet than in dry condition, inducing a lower response.

The role of sodium in enhancing the CO_2 detection relies on the increase in the concentration of oxygen vacancies as confirmed by XPS analysis (see **Table 2** and **Figure 2**), according to the following reaction [69]:

$$CO_2\,(ads) + V_O^{\cdot} \rightarrow CO_2^{\cdot} + V_O^X \quad (8)$$

where, $V_O^{\cdot}$ denote singly ionized oxygen vacancy and V_O^X denote neutral oxygen vacancy. On the one hand, whereas oxygen vacancies are additional surface sites of high reactivity, sodium could itself prove to be a promoter of the catalytic effect [70], causing both electronic and redox changes in the material.

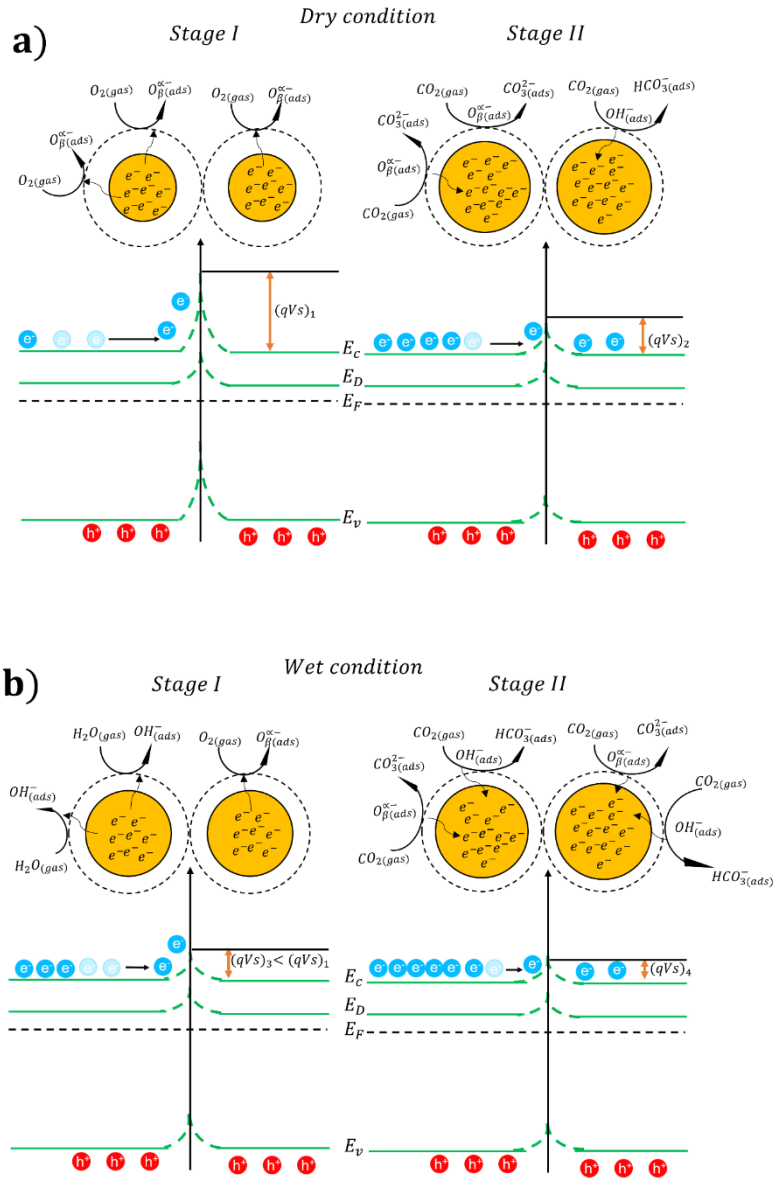

Figure 9. Reaction mechanisms on the surface a) in dry air (*Stage I*) and under CO_2 exposure (*Stage II*), and b) in wet air (*Stage I*) and under CO_2 exposure (*Stage II*). E_c and E_v are the conduction and valence bands, E_F is the Fermi level and E_D is the donor level created due to the doping by Na.

3. Conclusion

In this work, Na:In_2O_3 nanostructured powder was synthesized by sol-gel method. Extensive characterization by SEM, TEM, XRD, XPS and UV-vis confirmed the nanostructured nature of the material as spherical particles and the presence of sodium dispersed in the crystalline structure. Indeed, aggregates or second phases were not observed by TEM and XRD analysis, suggesting that the addition of sodium is properly distributed. In particular, XPS revealed an increase in the concentration of oxygen vacancies in the doped sample as compared to the pristine one, which turned out to magnify the surface reactivity of doped material. Indeed, Na:In_2O_3 was capable of reducing CO_2, suggesting that it can straight be used as a gas sensor.
The sensing performance was evaluated by investigating the sensitivity in dry and in RH% conditions, repeatability, and selectivity. In particular, the negligible influence of humidity enables the new MOX-based sensing material to a wide scenario of possible applications.
By comparing the performance to other CO_2 sensors in the literature, it emerged that Na:In_2O_3 as a functional material is very effective for CO_2 sensing at low temperature. In order to achieve additional information on the surface reaction mechanism of Na:In_2O_3-based gas sensors to CO_2, we performed *operando* DRIFT spectroscopy measurements. It was highlighted that the adsorption of CO_2 on the surface led to the formation of carbonate species, which, in the case of wet condition, compete with hydroxyl groups on the film. In order to further investigate this process, it might be necessary to conduct H_2O/D_2O and $^{12}CO/^{13}CO$ isotope exchange experiments to discriminate the different groups on the surface.
Therefore, the enhancement of oxygen vacancies caused by sodium doping was fundamental to increase the reactivity vs. CO_2. In order to deeply explore the role of sodium in the sensing mechanism, density functional theory calculations might provide significant information on the electronic structure and energy of interactions.
These sensing capabilities, corroborated by the technological advantage to operate at low temperature and the possible miniaturization for IoT networks, make the material investigated in this work the most effective MOX-based gas sensor for CO_2 detection, competing with widespread optical sensors.

4. Experimental Section

4.1. Materials

Indium (III) nitrate hydrate (99,9%) (In $(NO_3)_3$ x $5H_2O$) was purchased from Sigma-Aldrich, USA. Sodium hydroxide anhydrous pellets (NaOH), ammonia (NH_3) and propan-2-ol (C_3H_8O) were purchased from CARLO ERBA Reagents S.A.S.. Deionized water (DI) was procured from Millipore DI water purification system.

4.2. Synthesis and Film Deposition

Synthesis of Na:In_2O_3 powder. Na:In_2O_3 powder was synthetized through sol-gel technique. First, 0.1 M of $In(NO_3)_3$ x $5H_2O$ was dissolved in 60 ml of DI water. Then, 0.5 M of NaOH were added to the above precursor solution and stirred for 40 min at 70 °C.
Synthesis of In_2O_3 powder. In_2O_3 nanopowder was prepared by the sol-gel method. 0.1 M of $In(NO_3)_3$ x $5H_2O$ was dissolved in 60 ml of DI water. Then, 4.0 ml of NH_3 were added to the previously prepared solution. The mixture was stirred for 30-40 minutes at room temperature. The slurry, obtained from the two syntheses, was washed with iso-propanol and DI several times using a centrifuge at 5000 rpm for 2 min. The white precipitate was dried at 100 °C for 4 h and consecutively at 200 °C for 2 h. The dried powder was thermally treated at 450 °C for 3h in ambient air. The yellow powder was ground in an agate mortar and mixed with α-terpineol, ethyl cellulose and silica to form a homogeneous paste.
Film deposition. The resulting composites were screen printed onto alumina substrates with interdigitated gold electrodes on the front-side, and a platinum heater on the backside to thermo-activate the sensing layer of the device. The printed film was calcined at 450 °C for 3 h in air and finally packaged by bonding the four contacts to a TO-39 support using gold wires with a diameter of 0.06 mm [71].

4.3. Characterization of the materials

Scanning electron microscopy. The morphology of the obtained material was investigated by SEM using a Zeiss LEO 1530 FEG microscope, equipped with a Oxford Inst. INCA 250 30 mm^2 SSD EDX spectrometer.
Transmission electron microscopy. Microstructural and compositional analyses were performed by using a Philips TECNAI F20 ST TEM operating at 200 kV. The instrument was equipped with a EDAX SUTW EDX spectrometer and Fischione Inst. High-Angle Annular Dark-Field STEM imaging detector. TEM images were acquired in phase contrast mode. The sample was ground and suspended in iso-propanol solution and sonicated. Then a few drops of the solution were drop casting over a molybdenum grid and dried on a heating plate.
X-ray diffraction. XRD data collection was performed on a Bruker D8 Advance Da Vinci diffractometer working in Bragg-Brentano geometry, and equipped with a Cu-anode X-ray tube, Ni-filter to suppress the Cu $K\beta$ component, and a LynxEye XE silicon strip detector (angular range covered by the detector = 2.585° 2θ) set to discriminate Cu $K\alpha_{1,2}$ radiation. The powder was loaded in a 2 mm-deep cavity in a poly (methyl methacrylate) specimen holder and scanned in a continuous mode from 5 to 90° 2θ, with step size of 0.02° 2θ and a counting time of 2 s per step. Qualitative phase analysis of collected patterns was performed by means of the Bruker AXS EVA software (v.6.0.0.7). Collected XRPD patterns were modeled by means of the fundamental-parameter Rietveld approach (TOPAS v.5.0, Bruker).
X-ray photoelectron spectroscopy. XPS measurements were performed using a Kratos AXIS Ultra^{DLD} instrument (Kratos Analytical, Manchester, UK) equipped with a hemispherical analyzer and a monochromatic X-ray source Al Kα (1486.6 eV), in spectroscopy mode. For the measurements, powders were deposited on carbon tape, placed on a silicon support. Samples were analyzed using a 0° take-off angle between the sample surface normal and the analyzer axis, corresponding to a sampling depth of approximately 10 nm. The surveys were recorded to identify the elements present on the surface. High-resolution spectra of the core

levels of In, O and Na were collected for each sample. For the fit of the O 1s peaks we used a weighted sum of a Lorentzian and a Gaussian with a ratio of 0.25. XPS quantification was performed using the instrument sensitivity factors and high-resolution spectra. The alignment was performed by setting the hydrocarbon peak in the C 1s core level peak at 285 eV. All XPS data were analyzed using the software described elsewhere [72].

Optical absorption analysis. UV-visible measurements were performed by using a JASCO V-670 dual beam spectrophotometer. The instrument is equipped with a deuterium lamp (190-350 nm) and a halogen lamp (330-2700 nm). The measurements were performed in the wavelength range 200-800 nm, with a sampling interval of 1 nm. In order to carry out the analysis, the powder was dispersed in 2-propanol and subjected to an ultrasonic treatment for 30 minutes. The band gap of the powders was calculated using the Tauc Plot method, i.e., by calculating and adapting the absorption data of the nanopowders with respect to the direct transition energy:

$$\alpha h\nu = A\,(h\nu - E_g)^{\frac{1}{2}} \tag{10}$$

where α is the optical absorption coefficient, $h\nu$ is the energy of the photon, E_g is the direct band gap and A is a constant [73]. Plotting the graph of $(\alpha h\nu)^2$ as a function of the photon energy and extrapolating the linear portion of the curve up to zero absorption, the values of the E_g of the investigated materials were obtained.

4.4. Gas Sensing Measurements

The electrical characterization was developed through two approaches, in order to deeply investigate the gas sensing performance of In_2O_3-based sensors:

- *Electrical characterization:* experimentation in a standard test chamber for identifying the optimal working conditions, sensitivity, repeatability, response and recovery times, humidity influence and selectivity.
- *Sensing mechanism investigation:* operando DRIFT investigation of the Na:In_2O_3 sensor exposed to CO_2 in dry and wet conditions.

4.4.1. Electrical Characterization Setup

The sensing properties of Na:In_2O_3 film were tested in a 622 cm^3 gas-flow sealed chamber. Synthetic air (20% O_2 and 80% N_2) and target gases from certified cylinders (N5.0 degree of purity) were mixed and fluxed through mass-flow controllers at 500 standard cc/min (sccm). Then, the filling time of the test chamber was calculated to be about 1 minute and 15 seconds, as it depends on the size, geometry of the chamber and the velocity of the gas flow [46].

Relative humidity and temperature inside the test chamber were controlled by a commercial Honeywell HIH-4000 humidity sensor. The test chamber was placed in a climatic box, which maintains a constant outer temperature of 25 °C through a thermal ventilation system [74].

4.4.2. Electrical characterization

Working temperature. Sensors were kept at their optimal working temperature, identified after a proper calibration with temperature ranging from 150 to 300 °C, under a continuous flow of synthetic air, until the thermodynamic steady state was attained. The sensor response was defined as:

$$R = \frac{(G_{gas} - G_{dry\ air})}{G_{dry\ air}} \quad (11)$$

where G_{gas} and G_{air} are the steady-states conductance in gas and in air, respectively. The response (τ_{res}) and recovery (τ_{rec}) times were calculated as the time needed to reach 90% of the steady response and the time to restore 90% of the baseline level, respectively.
Sensitivity. The film was exposed to increasing concentrations ranging from 250 to 5000 ppm of CO_2 in order to sound out different application scenarios.
Repeatability. Na:In_2O_3 film was exposed to four cycles of 400 and 1200 ppm of CO_2.
Humidity influences. The sensors were stabilized at the beginning of each measurement by keeping the sensors at their working temperature under a continuous flow (500 sccm) of wet air, in the range of 1–75% RH %, by fluxing part of the total flux through a bubbler filled with distilled water. After the stabilization, the sensors were exposed to the target gas.

$$R = \frac{(G_{gas} - G_{wet\ air})}{G_{wet\ air}} \quad (12)$$

Selectivity. The concentrations of selected gases were chosen according to NIOSH, ASHRAE and the average tested levels reported in the literature [8,53–56]. The k_s was defined as the ratio of the response value of the sensors to CO_2 and interfering gas, respectively.

$$k_s = \frac{R_{CO2}}{R_{interfering\ gas}} \quad (13)$$

4.4.3 Operando DRIFT measurements

The kinetics at the gas-solid surface was investigated through operando experiments employing a Bruker Vertex 70 V vacuum FT-IR spectrometer, equipped with a DRIFT accessory (Praying Mantis, Harrick Scientific Products Inc.) (**Figure S10, Supporting Information**). The characterization of In_2O_3-based sensors was investigated using a dedicated apparatus, including a customized sealed gas test chamber (IR dome with a void-volume of ≈ 0.5 cm^3) and a data acquisition system (Zefiro). All specifications about the system for gas injection, chamber characteristics, and electronics are given in the [30].
The single-channel spectrum is composed by the absorption caused by functional groups of species adsorbed on the surface and by the sensing material itself which, together with the diverse individual component of the spectrometer (optical elements, light source emission and detector non-linearity) affect the overall shape of the single channel DRIFT spectrum.

The spectra were acquired through a liquid nitrogen-cooled mercury cadmium tellurium (MCT) mid-band detector, with a spectral range from 850 to 4000 cm^{-1}. Absorbance spectra were calculated by using the equation:

$$A = log_{10} \frac{I\ sample\ (\lambda)}{I\ background\ (\lambda)} \quad (14)$$

where $I\ sample$ (λ) and $I\ background$ (λ) are the spectra of the sample and the background [30,31].

Characterization in dry and wet conditions. The samples were maintained at its proper working temperature (200 °C) overnight, then each spectrum was collected at a resolution of 4 cm^{-1} averaging 1024 scans with a beam spot size of 2.5 mm. All the optical bench settings and spectral data acquisition were performed through Bruker OPUS software.

Before the CO_2 exposure, the measuring chamber was kept in a constant flow of 100 sccm of synthetic dry air, while the sensor operating temperature was gradually increased with steps of 50 °C up to 200 °C. Each temperature step was maintained for as long as to allow thermodynamically stabilization of the surface. The surface reactivity of the sensor was evaluated after maintaining the device at 200 °C for 1 day under 100 sccm constant flow of synthetic dry air and an applied voltage between the electrodes of 1.0 V [75]. According to these conditions, we evaluated the spectral background for each reported measurement. After a stabilization of the baseline for a few hours, the device was exposed to a mixture of 1000 and 3500 ppm of CO_2 and synthetic air under dry (≈1% RH at 30 °C) and wet conditions (up to 22% RH at 30 °C).

Supporting Information

Supporting Information is available from the Wiley Online Library or from the author.

Acknowledgements

Funded POR FSE 2014/2020 by Regione Emilia-Romagna. Research Project for Technology Transfer and Business. *Integrated management of satellite data and ground IoT sensors aimed at sustainability in precision farming practices for regional crops of excellence.*

Conflict of Interest

The authors declare no conflict of interest.

References

[1] Y. Lin, Z. Fan, *Mater. Sci. Semicond. Process.* **2020**, *107*, 104820.
[2] M. Grote, I. Williams, J. Preston, *Atmos. Environ.* **2014**, *95*, 214.
[3] NASA, Understanding our planet to benefit humankind, https://climate.nasa.gov/, .
[4] R. Pitarma, G. Marques, B. R. Ferreira, *J. Med. Syst.* **2017**, *41*, 23.
[5] S. Shriram, K. Ramamurthy, S. Ramakrishnan, *Build. Environ.* **2019**, *149*, 58.
[6] R. Maddalena, M. J. Mendell, K. Eliseeva, W. R. Chan, D. P. Sullivan, M. Russell, U. Satish, W. J. Fisk, *Indoor Air* **2015**, *25*, 362.
[7] U. Satish, M. J. Mendell, K. Shekhar, T. Hotchi, D. Sullivan, S. Streufert, W. J. Fisk, *Environ. Health Perspect.* **2012**, *120*, 1671.
[8] Immediately Dangerous To Life or Health (IDLH) Values, Centers for Disease Control and Prevention, **1994**.
[9] Z. Peng, J. L. Jimenez, *Environ. Sci. Technol. Lett.* **2021**, *8*, 392.
[10] M. N. Anwar, A. Fayyaz, N. F. Sohail, M. F. Khokhar, M. Baqar, W. D. Khan, K. Rasool, M. Rehan, A. S. Nizami, *J. Environ. Manage.* **2018**, *226*, 131.
[11] P. Puligundla, J. Jung, S. Ko, *Food Control* **2012**, *25*, 328.
[12] L. Yu, Y. Li, H. Yu, K. Zhang, X. Wang, X. Chen, J. Yue, T. Huo, H. Ge, K. A. Alamry, H. M. Marwani, S. Wang, *Sens. Actuators B Chem.* **2018**, *266*, 717.
[13] T.-V. Dinh, I.-Y. Choi, Y.-S. Son, J.-C. Kim, *Sens. Actuators B Chem.* **2016**, *231*, 529.
[14] A. Bulbul, H. Kim, *Lab. Chip* **2015**, *15*, 94.
[15] T. A. Vincent, J. W. Gardner, *Sens. Actuators B Chem.* **2016**, *236*, 954.
[16] S. Keerthana, K. Rathnakannan, *J. Alloys Compd.* **2022**, *897*, 162988.
[17] N. Rajesh, J. C. Kannan, T. Krishnakumar, A. Bonavita, S. G. Leonardi, G. Neri, *Ceram. Int.* **2015**, *41*, 14766.
[18] S. Joshi, S. J. Ippolito, S. Periasamy, Y. M. Sabri, M. V. Sunkara, *ACS Appl. Mater. Interfaces* **2017**, *9*, 27014.
[19] C. A. Zito, T. M. Perfecto, A.-C. Dippel, D. P. Volanti, D. Koziej, *ACS Appl. Mater. Interfaces* **2020**, *12*, 17745.
[20] I. Djerdj, A. Haensch, D. Koziej, S. Pokhrel, N. Barsan, U. Weimar, M. Niederberger, *Chem. Mater.* **2009**, *21*, 5375.
[21] A. Prim, E. Pellicer, E. Rossinyol, F. Peiró, A. Cornet, J. R. Morante, *Adv. Funct. Mater.* **2007**, *17*, 2957.
[22] C. Wang, L. Yin, L. Zhang, D. Xiang, R. Gao, *Sensors* **2010**, *10*, 2088.
[23] D. Degler, U. Weimar, N. Barsan, *ACS Sens.* **2019**, *4*, 2228.
[24] Y. Zhang, Y. Liu, L. Zhou, D. Liu, F. Liu, F. Liu, X. Liang, X. Yan, Y. Gao, G. Lu, *Sens. Actuators B Chem.* **2018**, *273*, 991.
[25] B. Liang, H. Duan, T. Sun, J. Ma, X. Liu, J. Xu, X. Su, Y. Huang, T. Zhang, *ACS Sustain. Chem. Eng.* **2019**, *7*, 925.
[26] J. Wang, G. Zhang, J. Zhu, X. Zhang, F. Ding, A. Zhang, X. Guo, C. Song, *ACS Catal.* **2021**, *11*, 1406.
[27] N. Sui, P. Zhang, T. Zhou, T. Zhang, *Sens. Actuators B Chem.* **2021**, *336*, 129612.
[28] X. Xu, D. Wang, W. Wang, P. Sun, J. Ma, X. Liang, Y. Sun, Y. Ma, G. Lu, *Sens. Actuators B Chem.* **2012**, *171–172*, 1066.
[29] T. Waitz, T. Wagner, T. Sauerwald, C.-D. Kohl, M. Tiemann, *Adv. Funct. Mater.* **2009**, *19*, 653.
[30] M. Valt, M. D. Ciana, B. Fabbri, D. Sali, A. Gaiardo, V. Guidi, *Sens. Actuators B Chem.* **2021**, *341*, 130012.
[31] M. D. Ciana, M. Valt, B. Fabbri, A. Gaiardo, E. Spagnoli, S. Krik, P. Bernardoni, N. Gilli, A. Migliori, A. Quaranta, V. Morandi, V. Guidi, *Sens. Actuators B Chem.* **2022**, *371*, 132497.

[32] A. Gurlo, R. Riedel, *Angew. Chem. Int. Ed.* **2007**, *46*, 3826.
[33] E. J. Mittemeijer, P. Scardi, Eds., *Diffraction Analysis of the Microstructure of Materials*, Vol. 68, Springer Berlin Heidelberg, Berlin, Heidelberg, **2004**.
[34] D. V. Shinde, D. Y. Ahn, V. V. Jadhav, D. Y. Lee, N. K. Shrestha, J. K. Lee, H. Y. Lee, R. S. Mane, S.-H. Han, *J Mater Chem A* **2014**, *2*, 5490.
[35] B. Hu, M. Hu, Q. Guo, K. Wang, X. Wang, *Appl. Catal. B Environ.* **2019**, *253*, 77.
[36] Y. Qi, L. Song, S. Ouyang, X. Liang, S. Ning, Q. Zhang, J. Ye, *Adv. Mater.* **2020**, *32*, 1903915.
[37] F. Shan, H.-Z. Sun, J.-Y. Lee, S. Pyo, S.-J. Kim, *IEEE Access* **2021**, *9*, 44453.
[38] R. Xing, L. Xu, J. Song, C. Zhou, Q. Li, D. Liu, H. Wei Song, *Sci. Rep.* **2015**, *5*, 10717.
[39] H. Idriss, *Surf. Sci.* **2021**, *712*, 121894.
[40] R. Jaisutti, M. Lee, J. Kim, S. Choi, T.-J. Ha, J. Kim, H. Kim, S. K. Park, Y.-H. Kim, *ACS Appl. Mater. Interfaces* **2017**, *9*, 8796.
[41] J. J. Carey, M. Nolan, *J. Mater. Chem. A* **2017**, *5*, 15613.
[42] K. Karmakar, A. Sarkar, K. Mandal, G. G. Khan, *ChemElectroChem* **2018**, *5*, 1147.
[43] T. Suzuki, H. Watanabe, T. Ueno, Y. Oaki, H. Imai, *Langmuir* **2017**, *33*, 3014.
[44] K. Anand, J. Kaur, R. C. Singh, R. Thangaraj, *Ceram. Int.* **2016**, *42*, 10957.
[45] R. Prakash, S. Kumar, F. Ahmed, C. G. Lee, J. I. Song, *Thin Solid Films* **2011**, *519*, 8243.
[46] E. Spagnoli, A. Gaiardo, B. Fabbri, M. Valt, S. Krik, M. Ardit, G. Cruciani, M. Della Ciana, L. Vanzetti, G. Vola, S. Gherardi, P. Bellutti, C. Malagù, V. Guidi, *ACS Sens.* **2022**, *7*, 573.
[47] O. Ramalho, G. Wyart, C. Mandin, P. Blondeau, P.-A. Cabanes, N. Leclerc, J.-U. Mullot, G. Boulanger, M. Redaelli, *Build. Environ.* **2015**, *93*, 115.
[48] M. Pavani, P. T. Rao, In *2016 IEEE 7th Annual Information Technology, Electronics and Mobile Communication Conference (IEMCON)*, IEEE, Vancouver, BC, Canada, **2016**, pp. 1–6.
[49] G. Chen, B. Han, S. Deng, Y. Wang, Y. Wang, *Electrochimica Acta* **2014**, *127*, 355.
[50] Y. Wang, K. Zhang, J. Zou, X. Wang, L. Sun, T. Wang, Q. Zhang, *Carbon* **2017**, *117*, 263.
[51] A. Gaiardo, B. Fabbri, A. Giberti, M. Valt, S. Gherardi, V. Guidi, C. Malagù, P. Bellutti, G. Pepponi, D. Casotti, G. Cruciani, G. Zonta, N. Landini, M. Barozzi, S. Morandi, L. Vanzetti, R. Canteri, M. Della Ciana, A. Migliori, E. Demenev, *Sens. Actuators B Chem.* **2020**, *305*, 127485.
[52] V. Galstyan, N. Poli, A. D'Arco, S. Macis, S. Lupi, E. Comini, *J. Mater. Chem. A* **2020**, *8*, 20373.
[53] J. G. Allen, P. MacNaughton, U. Satish, S. Santanam, J. Vallarino, J. D. Spengler, *Environ. Health Perspect.* **2016**, *124*, 805.
[54] S. C. Lee, M. Chang, *Indoor Air* **1999**, *9*, 134.
[55] C.-C. Jung, P.-C. Wu, C.-H. Tseng, H.-J. Su, *Build. Environ.* **2015**, *85*, 190.
[56] A. U. Raysoni, T. H. Stock, J. A. Sarnat, M. C. Chavez, S. E. Sarnat, T. Montoya, F. Holguin, W.-W. Li, *Environ. Pollut.* **2017**, *231*, 681.
[57] Y. Xia, A. Pan, Y.-Q. Su, S. Zhao, Z. Li, A. K. Davey, L. Zhao, R. Maboudian, C. Carraro, *Sens. Actuators B Chem.* **2022**, *357*, 131359.
[58] C. Li, Y. Sakata, T. Arai, K. Domen, K. Maruya, T. Onishi, *J. Chem. Soc. Faraday Trans. 1 Phys. Chem. Condens. Phases* **1989**, *85*, 929.
[59] I. Boehme, U. Weimar, N. Barsan, *Sens. Actuators B Chem.* **2021**, *326*, 129004.
[60] T. Suzuki, A. Sackmann, A. Oprea, U. Weimar, N. Bârsan, *ACS Sens.* **2020**, *5*, 2555.
[61] I. Can, U. Weimar, N. Barsan, In *Proceedings of Eurosensors 2017, Paris, France, 3–6 September 2017*, MDPI, **2017**, p. 432.
[62] E.-M. Köck, M. Kogler, T. Bielz, B. Klötzer, S. Penner, *J. Phys. Chem. C* **2013**, *117*, 17666.
[63] S. Harbeck, A. Szatvanyi, N. Barsan, U. Weimar, V. Hoffmann, *Thin Solid Films* **2003**, *436*, 76.

[64] T. Sahm, A. Gurlo, N. Bârsan, U. Weimar, *Sens. Actuators B Chem.* **2006**, *118*, 78.
[65] N. Barsan, D. Koziej, U. Weimar, *Sens. Actuators B Chem.* **2007**, *121*, 18.
[66] H. Ji, W. Zeng, Y. Li, *Nanoscale* **2019**, *11*, 22664.
[67] N. Barsan, U. Weimar, *J. Electroceramics* **2001**, *7*, 143.
[68] Y. Xiong, Q. Xue, C. Ling, W. Lu, D. Ding, L. Zhu, X. Li, *Sens. Actuators B Chem.* **2017**, *241*, 725.
[69] M. A. Basyooni, M. Shaban, A. M. El Sayed, *Sci. Rep.* **2017**, *7*, 41716.
[70] M. Konsolakis, M. Lykaki, *Catalysts* **2020**, *10*, 160.
[71] B. Fabbri, M. Valt, C. Parretta, S. Gherardi, A. Gaiardo, C. Malagù, F. Mantovani, V. Strati, V. Guidi, *Sens. Actuators B Chem.* **2020**, *303*, 127227.
[72] G. Speranza, R. Canteri, *SoftwareX* **2019**, *10*, 100282.
[73] L. Ye, L. Tian, T. Peng, L. Zan, *J. Mater. Chem.* **2011**, *21*, 12479.
[74] M. Valt, M. Caporali, B. Fabbri, A. Gaiardo, S. Krik, E. Iacob, L. Vanzetti, C. Malagù, M. Banchelli, C. D'Andrea, M. Serrano-Ruiz, M. Vanni, M. Peruzzini, V. Guidi, *ACS Appl. Mater. Interfaces* **2021**, *13*, 44711.
[75] M. Della Ciana, M. Valt, B. Fabbri, P. Bernardoni, V. Guidi, V. Morandi, *Rev. Sci. Instrum.* **2021**, *92*, 074702.